Understanding the Quantum Rabi Ring Using Analogies to Quantum Magnetism

Diego Fallas Padilla* and Han Pu†
Department of Physics and Astronomy, and Rice Center for Quantum Materials, Rice University, Houston, Texas 77251-1892, USA

Guo-Jing Cheng and Yu-Yu Zhang‡
Department of Physics, and Chongqing Key Laboratory for strongly coupled Physics, Chongqing University, Chongqing 401330, China

(Received 19 July 2022; accepted 26 September 2022; published 24 October 2022)

We map a quantum Rabi ring, consisting of N cavities arranged in a ring geometry, into an effective magnetic model containing the XY exchange and the Dzyaloshinskii-Moriya (DM) interactions. The analog of the latter is induced by an artificial magnetic field, which modulates photon hopping between nearest-neighbor cavities with a phase. This mapping facilitates the description and understanding of the different phases in the quantum optical model through simple arguments of competing magnetic interactions. For the square geometry ($N = 4$) the rich phase diagram exhibits three superradiant phases denoted as ferro-superradiant, antiferro-superradiant, and chiral superradiant. In particular, the DM interaction is responsible for the chiral phase in which the energetically degenerate configurations of the order parameters are similar to the in-plane magnetizations of skyrmions with different helicities. The antiferro-superradiant phase is suppressed in the triangle geometry ($N = 3$) as geometric frustration contributes to stabilize the chiral phase even for small values of the DM interaction. The chiral phases for odd and even N show a different scaling behavior close to the phase transition. The equivalent behavior on both systems opens the possibility of simulating chiral magnetism in a few-body quantum optical platform, as well as understanding one system using the insights gained from the other.

DOI: 10.1103/PhysRevLett.129.183602

Introduction.—It is not unusual that two seemingly very different systems are connected by the same underlying physics. Finding such connections can often help us to gain new insights into one system by importing knowledge obtained from the study of the other. Here we show how a light-matter interaction system—the quantum Rabi ring—can be mapped to a chiral magnetic system consisting of various kinds of magnetic couplings including, for example, the Dzyaloshinskii-Moriya (DM) interaction [1,2] which plays a fundamental role in the study of topological states in magnetic systems; see, for example, Ref. [3]. The DM interaction favors noncollinear spin structures, stabilizing interesting spin textures such as magnetic vortices and magnetic skyrmions in chiral magnets [4–6].

Unlike in real magnetic materials, in effective magnetic models obtained from the mapping of a distinct system, the relative strengths of the different magnetic interactions may be easily tuned. In particular, light-matter interaction platforms have been used to simulate antiferromagnetic spin chains [7] and frustrated classical magnetism [8] and to engineer collective spin exchange interactions [9]. High tunability and control make platforms such as cavity and circuit QED [10–13] and cold atoms [14–16] ideal to explore many-body quantum phases.

Richer behaviors can be achieved when external fields are added to the mix. Recent experimental advances and theoretical findings have addressed synthesizing magnetic fields for neutral ultracold atoms [17–19] and photonic systems [15,20–23]. In particular, addition of artificial magnetic fields has been proven to unlock the emergence of exotic phases of matter, such as chiral ground-state currents of interacting photons in a 3-qubit loop [22], chiral phases in a quantum Rabi triangle [24], and fractional quantum Hall physics in the Jaynes-Cummings Hubbard lattice [25–27].

Here, by mapping the quantum Rabi ring into a magnetic system, described by the Lipkin-Meshkov-Glick (LMG) model, the different phases in the former can be intuitively understood by studying the competition of the DM interaction and the XY Heisenberg exchange interaction, as well as the presence or absence of geometric frustration in the equivalent LMG ring.

Quantum Rabi ring.—We consider a system with N cavities placed in a ring. Each cavity contains a two-level atom and is described by the quantum Rabi Hamiltonian,

$$H_{R,n} = \omega a_n^\dagger a_n + g(a_n^\dagger + a_n)\sigma_n^x + \frac{\Delta}{2}\sigma_n^z, \qquad (1)$$

where a_n ($a_n^\dagger$) is the photon annihilation (creation) operator of the single-mode cavity with frequency ω at cavity n, g is the atom-cavity coupling strength, and σ_n^i are the Pauli

matrices representing the two-level atom at site n with energy splitting Δ between levels. The dimensionless coupling strength is defined as $g_1 \equiv g/\sqrt{\Delta\omega}$.

Although quantum phase transitions (QPTs) are often studied in the thermodynamic limit [28], some few-body systems such as the quantum Rabi model [29–36] have been proven to undergo QPTs in alternative limits such as the classical oscillator (CO) limit with $\Delta/\omega \to \infty$ [37]. This is the regime we will focus on in this work.

The quantum Rabi ring Hamiltonian contains photon hopping between the neighboring cavities,

$$H_{\mathrm{RR}} = \sum_{n=1}^{N} H_{R,n} + \sum_{n=1}^{N} J(e^{i\theta} a_n^\dagger a_{n+1} + e^{-i\theta} a_{n+1}^\dagger a_n), \tag{2}$$

where J is the hopping amplitude between nearest-neighbor cavities with a phase θ, and periodic boundary conditions imply $a_{N+1} = a_1$. A thorough description of this system in a triangle ($N = 3$) can be found in Ref. [24]. An artificial vector potential $A(r)$ leads the photon hopping terms between nearby cavities n and m to become complex with the phase given by $\theta = \int_{r_n}^{r_m} A(r)dr$. The artificial magnetic field can be realized by a periodic modulation of the photon hopping strength among the different cavities [22,24]. The complex phase breaks time-reversal symmetry and, as will be shown, is crucial in leading to the DM interaction in the mapped magnetic model.

In the CO limit, for small values of g_1, the average number of photons in the cavity tends to zero, which is the so-called normal phase. As g_1 increases to the critical point g_{1c}, the system undergoes a QPT as the photon population in each cavity becomes macroscopic (proportional to (Δ/ω)), signaling the superradiant phase. Moreover, the hopping of photons between neighboring cavities unlocks more exotic superradiant phases with the order parameter $\langle a_n \rangle$ being site dependent.

A general description of the mean-field features and excitation spectrum of this model can be done by constructing low-energy effective Hamiltonians for each phase (see Supplemental Material [38]). After shifting the bosonic operator $a_n \to \tilde{a}_n + \alpha_n$ with the complex mean-field value $\alpha_n = A_n + iB_n$, the effective low-energy Hamiltonian under the condition $J/\omega \ll 1$ is obtained by projecting to the spin subspace $|\downarrow\rangle$, giving

$$H_{\mathrm{eff}}^{\downarrow} = \sum_{n=1}^{N} \Big[\omega \tilde{a}_n^\dagger \tilde{a}_n - \frac{\lambda_n^2}{\Delta_n} (\tilde{a}_n^\dagger + \tilde{a}_n)^2 + J\tilde{a}_n^\dagger (e^{i\theta}\tilde{a}_{n+1} + e^{-i\theta}\tilde{a}_{n-1}) \Big] + E_g, \tag{3}$$

where $\Delta_n \equiv \sqrt{\Delta^2 + 16g^2A_n^2}$, $\lambda_n \equiv g\Delta/\Delta_n$, and the mean-field ground-state energy E_g is given by

$$E_g = \sum_{n=1}^{N} \Big[\omega(A_n^2 + B_n^2) - \frac{1}{2}\sqrt{\Delta^2 + 16g^2A_n^2} + 2J\cos\theta(A_nA_{n+1} + B_nB_{n+1}) + 2J\sin\theta(B_nA_{n+1} - B_{n+1}A_n) \Big]. \tag{4}$$

Minimization of E_g with respect to A_n and B_n [38] yields the mean-field values of A_n and B_n which depend strongly on N being odd or even, as shown later.

Effective magnetic model: LMG ring.—We now map the effective Hamiltonian (3) using the Holstein-Primakoff transformation [39] given by $S^z = a^\dagger a - S$ and $S_n^+ = a_n^\dagger\sqrt{2S - a_n^\dagger a_n}$. In the normal phase $\langle a_n \rangle = A_n + iB_n = 0$, and in the classical spin limit $S \to \infty$, the Holstein-Primakoff transformation can be approximated by $S_n^+ \approx \sqrt{2S}a_n^\dagger$, leading to the magnetic Hamiltonian:

$$H_{\mathrm{LMGR}} = \sum_{n=1}^{N} \Big[\omega S_n^z - \frac{2g_1^2\omega}{S}(S_n^x)^2 \Big] + \frac{J}{S}\cos\theta \sum_{n=1}^{N} (S_n^x S_{n+1}^x + S_n^y S_{n+1}^y) + \frac{J}{S}\sin\theta \sum_{n=1}^{N} \hat{z}\cdot(\vec{S}_n \times \vec{S}_{n+1}), \tag{5}$$

which is also valid for the region in the superradiant phase not too far away from the normal-superradiant phase boundary. We denote H_{LMGR} as the LMG ring model as it is a generalization of the LMG Hamiltonian [40] with additional nearest-neighbor interactions included. The physical meaning of each term in H_{LMGR} is quite clear: The two terms in the first line represent an external magnetic field along the z axis and the easy-axis anisotropy along the x axis, respectively; the second line is a typical XY spin exchange interaction which is either ferromagnetic or antiferromagnetic depending on the sign of $J\cos\theta$; finally, the last line corresponds to the DM interaction with the strength $J\sin\theta$. The relative strength between the XY and the DM terms is thus readily controlled by θ.

Treating $\vec{S}$ as a classical vector, the mean-field energy according to H_{LMGR} can be readily derived as

$$\frac{E_{\mathrm{MF}}}{\omega S} = \sum_{n=1}^{N} -\sqrt{(1 - X_n^2 - Y_n^2)} - 2g_1^2X_n^2 + \frac{J}{\omega}\cos\theta(X_nX_{n+1} + Y_nY_{n+1}) + \frac{J}{\omega}\sin\theta(X_nY_{n+1} - X_{n+1}Y_n), \tag{6}$$

where we have defined $X_n = (\langle S_n^x \rangle/S)$ and $Y_n = (\langle S_n^y \rangle/S)$. Minimization E_{MF} with respect to X_n and Y_n yields the

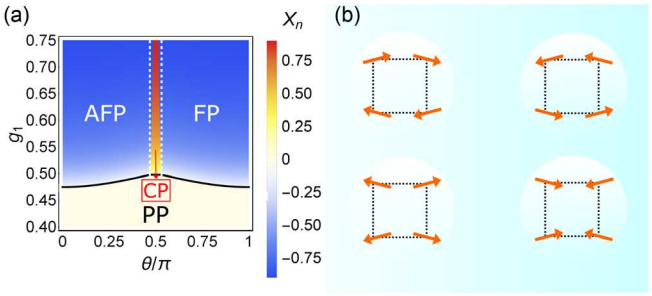

FIG. 1. (a) Phase diagram in the $\theta - g_1$ plane for the LMG ring with $N = 4$ using X_n for a given site n as order parameter. To facilitate visualization of the different phases we have chosen one of the degenerate configurations of the ground state for each phase, such that X_n in the chiral phase has opposite sign. The solid black line represents the second-order phase boundary, while vertical dashed lines represent the predicted first-order lines obtained from the equivalent quantum Rabi ring. (b) Allowed magnetization configurations in the CP for $N = 4$ represented in the xy plane. In all our calculations, we set $\Delta/\omega = 50$ and $J/\omega = 0.05$, as well as choosing $\omega = 1$ as the units for frequency.

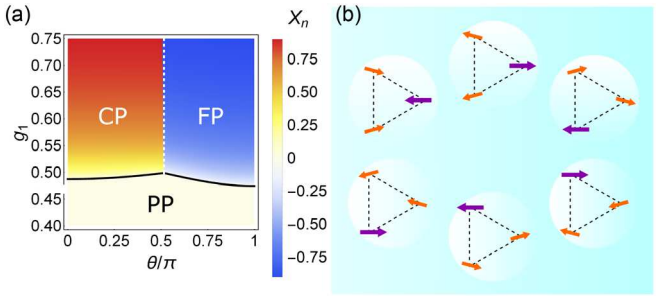

FIG. 2. (a) Phase diagram in the θ-g_1 plane for the LMG ring with $N = 3$; symbols are chosen as in Fig. 1(a). (b) Allowed magnetization configurations in the CP for $N = 3$ represented in the xy plane. Arrows with different color and length represent sites with different in-plane magnetization length $l_n = \sqrt{X_n^2 + Y_n^2}$.

ground-state phase diagram. One example with $N = 4$ is shown in Fig. 1(a). We only consider $\theta \in [0, \pi]$. The phase diagram in the range $\theta \in [-\pi, 0]$ is a mirror image of the one presented here.

For small g_1, the system is in the paramagnetic phase (PP) where the spin is polarized by external field term along the z axis. The PP is the analog of the normal phase in the original Rabi ring model. When g_1 exceeds a critical value, the system enters various nonparamagnetic phases according to the value of θ through a second-order phase transition. Defining two critical values of θ as

$$\cos\theta_c^{\pm} = \pm\frac{1 - \sqrt{1 + 16J^2/\omega^2}}{4J/\omega} \approx \mp 2J/\omega, \qquad (7)$$

the nonparamagnetic phases can be characterized as follows.

(1) Ferromagnetic phase (FP). For $\theta \in (\theta_c^+, \pi]$, and $g_1 > g_{1c}^{\mathrm{FP}} = \frac{1}{2}\sqrt{1 + (2J/\omega)\cos\theta}$, the system enters the FP. Here the XY coupling is ferromagnetic. Together with the easy-axis anisotropy term, it polarizes the spin along either the x or the $(-x)$ axis. The ground state in FP is doubly degenerate as a result of the break of the Z_2 symmetry.

(2) Antiferromagnetic phase (AFP). For $\theta \in [0, \theta_c^-)$, and $g_1 > g_{1c}^{\mathrm{AFP}} = \frac{1}{2}\sqrt{1 - (2J/\omega)\cos\theta}$, the system enters the AFP. Here the XY coupling is antiferromagnetic. The spins are polarized along the $(\pm x)$ axis and neighboring spins are antialigned. The ground state in AFP is also doubly degenerate.

(3) Chiral magnetic phase (CP). In between FP and AFP, for $\theta \in (\theta_c^-, \theta_c^+)$ and $g_1 > g_{1c}^{\mathrm{CP}} = \frac{1}{2}\sqrt{1 + (4J^2/\omega^2)\sin^2\theta}$, the DM term dominates over the XY coupling and renders spins at different sites no longer collinear. Here the ground state is fourfold degenerate, breaking both the Z_2 and the C_4 symmetries, and the corresponding in-plane magnetization orientation in the xy plane is shown in Fig. 1(b).

Note that the transitions between various nonparamagnetic phases are all of first order, and the critical points at $\theta_c^{\pm}$ are triple points where three phases (PP, FP or AFP, and CP) coexist.

Each magnetic phase described in terms of the values of X_n and Y_n has an equivalent phase in the quantum Rabi ring in terms of A_n and B_n, as shown in Table I. A similar phase diagram as in Fig. 1(a) would be obtained if we solve the quantum Rabi ring Hamiltonian (3) directly. In particular, the second-order phase boundary between the normal and the superradiant phases is exactly the same as the boundary between the paramagnetic and nonparamagnetic phases. The first-order phase boundaries between different superradiant phases slightly deviates from those between different nonparamagnetic phases for large g_1 far away from the second-order boundary.

The similarity in the mean-field behavior of both systems indicates the possibility of simulating magnetic behavior using the quantum Rabi ring, at the same time it opens the possibility of understanding better the chiral phases in the quantum Rabi ring by comparing them with the well-understood features of chiral magnetism. In addition to

TABLE I. Correspondence between phases in the quantum Rabi ring (QRR) and those in the LMG ring (LMGR).

QRR phase	LMGR phase
Normal: $A_n = B_n = 0$	Paramagnetic: $X_n = Y_n = 0$
Ferro-superradiant: $B_n = 0$ and $A_n = A_{n+1}$	Ferromagnetic: $Y_n = 0$ and $X_n = X_{n+1}$
Antiferro-superradiant: $B_n = 0$ and $A_n = -A_{n+1}$	Antiferromagnetic: $Y_n = 0$ and $X_n = -X_{n+1}$
Chiral superradiant: $B_n \neq 0$ and $A_n \neq 0$	Chiral magnetic: $Y_n \neq 0$ and $X_n \neq 0$

realizing various types of magnetic coupling terms, we can also simulate geometric frustration by changing N from even to odd. To this end, let us consider a triangular system with $N = 3$. Such an arrangement with antiferromagnetic coupling is a prototypical system that exhibits magnetic frustration.

The phase diagram for $N = 3$ is shown in Fig. 2(a). We can use the same conceptual reasoning of competing magnetic interactions to understand the phase diagram of this particular geometry. The FP has identical expressions for the second-order phase boundary and order parameter values as the ones found for $N = 4$. However, the AFP region is reduced to the line $\theta = 0$. Along this line, the DM interaction vanishes exactly and the spins are aligned in the x direction with the behavior being exactly the one of a classical frustrated antiferromagnet described by a Heisenberg model, as pointed out recently [41].

The CP is much broader in the triangular case as it is defined in the region where $0 < \theta \leq \theta_c = \cos^{-1}(-(2J/\sqrt{8J^2+\omega^2}+\omega))$ [24]. The ground state in the CP is sixfold degenerate due to the break of both the Z_2 and the C_3 symmetries. The in-plane magnetization orientation of the degenerate CP states are shown in Fig. 2(b). In the previous square case, the spins at different sites point along different directions, but all have the same length. This is not the case in the triangular case. As one can see from Fig. 2(b), there is always a site where the transverse spin is along the x or $(-x)$ axis and this spin has larger magnitude than the other two. In the triangular quantum Rabi ring model, this means that the photon numbers at different sites are not the same. This has important consequences in the excitation spectrum, as we will show later. Also note that, for small values of θ, the XY exchange interaction $J\cos\theta > 0$ is stronger than the DM interaction; however, the system still favors a chiral phase with noncollinear alignment. This is very much in line with observations in antiferromagnetic systems [42–44] where geometric frustration has been proven to stabilize chiral spin textures favored by the DM interaction, even for very small values of the coupling strength.

Excitation energy scaling.—To characterize the differences between chiral phase transitions with and without frustration, we analyze the excitation energy behavior near the transition for $N = 3$ and $N = 4$. The effective Hamiltonian in Eq. (3) can be diagonalized as $H_{\text{eff}}^{\downarrow} = \sum_{n=1}^{N} \varepsilon_n b_n^\dagger b_n$ [38], where ε_n is the excitation energy of the nth mode and b_n ($b_n^\dagger$) are bosonic annihilation (creation) operators of such mode obtained through a Bogoliubov transformation. Across a second-order phase boundary we expect the lowest excitation energy ε_1 to vanish exactly at the critical point, with a power-law behavior of the form $\varepsilon_1 \propto |g_1 - g_{1c}|^\gamma$ around the critical point g_{1c}. Usually, it is expected that the value of γ is independent of whether the critical point is approached from above or below. However, as discussed below, this is not the case for the frustrated phases.

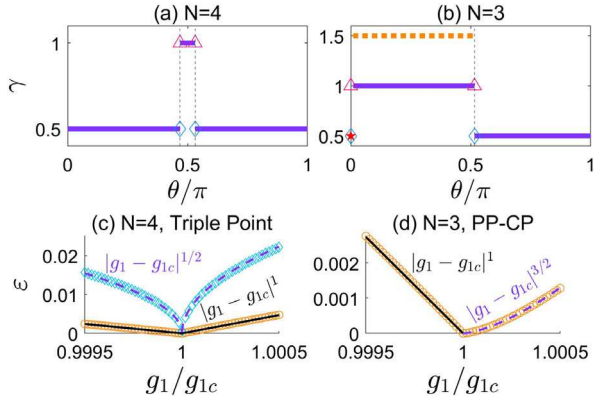

FIG. 3. Scaling exponents γ as a function of θ for (a) $N = 4$ and (b) $N = 3$; vertical dashed lines indicate the boundary between nonparamagnetic phases. At the triple points, two modes vanish at the critical point with distinct exponents indicated with open markers and a red star. The PP-CP transition for $N = 3$ in (b) has nonsymmetric exponents; the purple solid and the orange dashed line indicate the exponent when g_1 approaches the critical value from below and above, respectively. (c) Lowest and second-lowest excitation energies as a function of g_1/g_{1c} across the triple point at $\theta = \theta_c^+$. (d) Lowest excitation energy as a function of g_1/g_{1c} across the PP and the CP boundary for $N = 3$. Open markers signal the numerical results while the fitting functions are denoted by dashed and solid lines.

The scaling exponents γ as a function of θ are shown in Figs. 3(a) and 3(b) for $N = 4$ and $N = 3$, respectively. For $N = 4$ the scaling exponents before and after the transition are always equal to each other. The PP-FP and PP-AFP transitions have the same scaling exponent $\gamma = 1/2$, which is the same as the conventional single-cavity Dicke transition [45]. By contrast, $\gamma = 1$ for the PP-CP transition. At the triple point, two modes should vanish at the critical point as a signature of the coexistence of both nonparamagnetic phases; see Fig. 3(c). These modes possess exponents 1 and $1/2$, respectively, as indicated by the open markers in Fig. 3(a).

For $N = 3$ in the PP-FP transition $\gamma = 1/2$ just as in the $N = 4$ case. However, the PP-CP transition has an unusual scaling behavior as a consequence of the frustrated ground-state configurations. As shown in Fig. 3(b) and in more detail in Fig. 3(d), the exponents at the two sides of the phase transition are different: $\gamma = 1$ $(= 1.5)$ for g_1 approaching g_{1c} from below (above). At the triple point, we again have two modes vanishing at the critical point, each of which has a well-defined scaling exponent, given by $\gamma = 1$ and $\gamma = 1/2$, just as for $N = 4$.

The difference in the scaling behavior of the CP for $N = 3$ and 4 can be understood by exploring Eq. (3). For $N = 3$, Hamiltonian (3) is C_3 symmetric for $g_1 < g_{1c}$ as λ_n/Δ_n is independent of n. However, for $g_1 > g_{1c}$, one of the sites has a different value of λ_n/Δ_n, breaking the symmetry.

For $N = 4$, on the other hand, A_n^2 is independent of n in all phases, and consequently, Eq. (3) is always C_4 symmetric for both normal (paramagnetic) and superradiant (nonparamagnetic) phases.

This nonsymmetric scaling behavior as a consequence of frustration has been reported for the special point $\theta = 0$ [41] where two modes vanish at the critical point, one with a single exponent $1/2$ and the other with nonsymmetric exponents $\gamma = 1/2$ and $\gamma = 1$ below and above the transition; these three exponents are signaled in Fig. 3(b). This is consistent with our results as the point $\theta = 0$ in our model where θ is a variable represents a triple point between the frustrated AFP and the frustrated *CP*, then, the vanishing of two modes is expected. Moreover, the nonsymmetric γ values ($1/2$ and 1) at this point are different from the ones inside the *CP* region (1 and 1.5) as the ground-state configurations at $\theta = 0$ are not chiral, even though they are still frustrated.

Conclusions.—We have explored the connection between the quantum Rabi ring model and a magnetic model (LMG ring) containing the *XY* exchange and the DM interactions.

Our work illustrates how new exotic chiral phases of light can be better understood by borrowing well-known concepts from chiral magnetism. Moreover, it opens new possibilities in simulating magnetic systems using quantum optical platforms whose parameters can be much more readily tuned. In particular, the classical oscillator limit considered here facilitates the study of systems consisting of only a few (small N) spins, which can be a powerful tool for identifying the building blocks of more complex behaviors in real materials.

H. P. acknowledges support from the U.S. NSF and the Welch Foundation (Grant No. C-1669). Y.-Y. Z. acknowledges support from NSFC under Grants No. 12075040 and No. 12147102, Chongqing NSF under Grant No. cstc2020jcyj-msxmX0890, and Fundamental Research Funds for the Central Universities Grant No. 2021CDJQY-007.

Note added.—Recently, an article [46] appeared where the authors studied a similar system.

*daf5@rice.edu
†hpu@rice.edu
‡yuyuzh@cqu.edu.cn

[1] I. Dzyaloshinsky, J. Phys. Chem. Solids **4**, 241 (1958).
[2] T. Moriya, Phys. Rev. **120**, 91 (1960).
[3] N. Nagaosa and Y. Tokura, Nat. Nanotechnol. **8**, 899 (2013).
[4] A. Bogdanov and D. Yablonskii, Zh. Eksp. Teor. Fiz. **95**, 182 (1989).
[5] A. Bogdanov and A. Hubert, J. Magn. Magn. Mater. **138**, 255 (1994).
[6] U. K. Roessler, A. Bogdanov, and C. Pfleiderer, Nature (London) **442**, 797 (2006).
[7] J. Simon, W. S. Bakr, R. Ma, M. E. Tai, P. M. Preiss, and M. Greiner, Nature (London) **472**, 307 (2011).
[8] J. Struck, C. Ölschläger, R. Le Targat, P. Soltan-Panahi, A. Eckardt, M. Lewenstein, P. Windpassinger, and K. Sengstock, Science **333**, 996 (2011).
[9] M. A. Norcia, R. J. Lewis-Swan, J. R. Cline, B. Zhu, A. M. Rey, and J. K. Thompson, Science **361**, 259 (2018).
[10] A. D. Greentree, C. Tahan, J. H. Cole, and L. C. Hollenberg, Nat. Phys. **2**, 856 (2006).
[11] M. J. Hartmann, F. G. Brandao, and M. B. Plenio, Nat. Phys. **2**, 849 (2006).
[12] C. J. Zhu, L. L. Ping, Y. P. Yang, and G. S. Agarwal, Phys. Rev. Lett. **124**, 073602 (2020).
[13] S. Felicetti and A. Le Boité, Phys. Rev. Lett. **124**, 040404 (2020).
[14] I. Bloch, J. Dalibard, and W. Zwerger, Rev. Mod. Phys. **80**, 885 (2008).
[15] H. Cai and D.-W. Wang, Natl. Sci. Rev. **8**, nwaa196 (2021).
[16] X. Chen, Z. Wu, M. Jiang, X.-Y. Lü, X. Peng, and J. Du, Nat. Commun. **12**, 6281 (2021).
[17] Y.-J. Lin, R. L. Compton, K. Jiménez-García, J. V. Porto, and I. B. Spielman, Nature (London) **462**, 628 (2009).
[18] J. Dalibard, F. Gerbier, G. Juzeliūnas, and P. Öhberg, Rev. Mod. Phys. **83**, 1523 (2011).
[19] H. Cao, Q. Wang, and L.-B. Fu, Phys. Rev. A **89**, 013610 (2014).
[20] R. O. Umucalılar and I. Carusotto, Phys. Rev. Lett. **108**, 206809 (2012).
[21] D.-W. Wang, H. Cai, R.-B. Liu, and M. O. Scully, Phys. Rev. Lett. **116**, 220502 (2016).
[22] P. Roushan, C. Neill, A. Megrant, Y. Chen, R. Babbush, R. Barends, B. Campbell, Z. Chen, B. Chiaro, A. Dunsworth *et al.*, Nat. Phys. **13**, 146 (2017).
[23] I. Bloch, J. Dalibard, and S. Nascimbene, Nat. Phys. **8**, 267 (2012).
[24] Y.-Y. Zhang, Z.-X. Hu, L. Fu, H.-G. Luo, H. Pu, and X.-F. Zhang, Phys. Rev. Lett. **127**, 063602 (2021).
[25] A. L. C. Hayward, A. M. Martin, and A. D. Greentree, Phys. Rev. Lett. **108**, 223602 (2012).
[26] A. L. C. Hayward and A. M. Martin, Phys. Rev. A **93**, 023828 (2016).
[27] C. Noh and D. G. Angelakis, Rep. Prog. Phys. **80**, 016401 (2017).
[28] S. Sachdev, *Quantum Phase Transitions*, 2nd ed. (Cambridge University Press, Cambridge, England, 2011).
[29] M.-J. Hwang, R. Puebla, and M. B. Plenio, Phys. Rev. Lett. **115**, 180404 (2015).
[30] M. Liu, S. Chesi, Z.-J. Ying, X. Chen, H.-G. Luo, and H.-Q. Lin, Phys. Rev. Lett. **119**, 220601 (2017).
[31] X.-Y. Chen, Y.-Y. Zhang, L. Fu, and H. Zheng, Phys. Rev. A **101**, 033827 (2020).
[32] D. Braak, Phys. Rev. Lett. **107**, 100401 (2011).
[33] Q.-H. Chen, C. Wang, S. He, T. Liu, and K.-L. Wang, Phys. Rev. A **86**, 023822 (2012).
[34] X.-Y. Chen and Y.-Y. Zhang, Phys. Rev. A **97**, 053821 (2018).
[35] M.-J. Hwang and M. B. Plenio, Phys. Rev. Lett. **117**, 123602 (2016).

[36] S. Ashhab, Phys. Rev. A **87**, 013826 (2013).
[37] L. Bakemeier, A. Alvermann, and H. Fehske, Phys. Rev. A **85**, 043821 (2012).
[38] See Supplemental Material at http://link.aps.org/supplemental/10.1103/PhysRevLett.129.183602 for more details on the derivation of the effective Hamiltonians and phase boundaries.
[39] T. Holstein and H. Primakoff, Phys. Rev. **58**, 1098 (1940).
[40] H. J. Lipkin, N. Meshkov, and A. Glick, Nucl. Phys. **62**, 188 (1965).
[41] J. Zhao and M.-J. Hwang, Phys. Rev. Lett. **128**, 163601 (2022).
[42] S. Hayami, S.-Z. Lin, and C. D. Batista, Phys. Rev. B **93**, 184413 (2016).
[43] M. Mohylna, J. Buša, Jr., and M. Žukovič, J. Magn. Magn. Mater. **527**, 167755 (2021).
[44] H. D. Rosales, D. C. Cabra, and P. Pujol, Phys. Rev. B **92**, 214439 (2015).
[45] C. Emary and T. Brandes, Phys. Rev. E **67**, 066203 (2003).
[46] J. Zhao and M.-J. Hwang, arXiv:2208.02268.